

A Heuristic Quantum-Classical Algorithm for Modeling Substitutionally Disordered Binary Crystalline Materials

Tanvi P. Gujarati,¹ Tyler Takeshita,² Andreas Hintennach,³ and Eunseok Lee^{2,4,*}

¹*IBM Research Almaden, San Jose, California 95120, USA*

²*Mercedes-Benz Research and Development North America, Sunnyvale, California 94085, USA*

³*Daimler AG, HPC G012, 45 Hanns-Klemm-Str., Boblingen 71034, Germany*

⁴*Department of Mechanical and Aerospace Engineering,
The University of Alabama in Huntsville, Huntsville, Alabama 35899*

(Dated: November 12, 2021)

Improving the efficiency and accuracy of energy calculations has been of significant and continued interest in the area of materials informatics, a field that applies machine learning techniques to computational materials data. Here, we present a heuristic quantum-classical algorithm to efficiently model the energy of substitutionally disordered binary crystalline materials. Specifically, a quantum circuit, that scales linearly in its parameters, is designed to predict the energies of quantum chemical simulations in an exponentially-scaling feature space. This circuit is trained by classical supervised-learning using data obtained from classically-computed quantum chemical simulations. The algorithm is able to detect and rectify anomalies in the data. The feasibility of the algorithm is demonstrated on the layer-structured Li-cobaltate system, a widely-used Li-ion battery cathode material component. The result shows that our quantum circuit model presents a suitable choice for modelling the energies obtained from a quantum mechanical system. Analysis of the anomalous data provides insights into the thermodynamic properties of the system studied.

I. INTRODUCTION

Materials informatics (MI) [1–3], a recent trend in computational materials science, is a field of study that applies machine learning techniques to materials data to efficiently predict material properties [4–8], ultimately aimed at accelerating materials development and deployment, e.g. for battery materials [9, 10].

One of the challenging tasks in MI is to construct sufficiently rich models that can describe material properties realistically; often requiring expensive computations and data management that is intractable with today’s computational resources [11–14]. A quantum computer may be an attractive candidate to mitigate these challenges by providing greatly improved computational power, represented by its potential to solve certain exponentially-scaling problems more efficiently. Although the ability to implement useful problems on current quantum computers is limited due to decoherence and errors [15–17], recent approaches [18–20] based on the hybridization of quantum and classical computing were successfully demonstrated on the quantum hardware currently in operation [21–28]. In these hybrid approaches, a single lengthy operation on a quantum processing unit is replaced with a series of shorter processes, which are less vulnerable to the decoherence and errors, and interleaved with classically computed calibration routines.

Aligned with these approaches, here we present a hybrid quantum-classical algorithm to model the energy of substitutionally disordered binary crystalline materials. More specifically, a quantum circuit that links the energy and atomic position of materials is designed and trained by supervised-learning based on classical data instances (the result of quantum chemical simulation from classical computations). The immediate advantage of using a quantum circuit model is the availability of a quantum mechanically enhanced feature space for data representation that can encode correlations generated due to quantum entanglement which a classical model cannot. Also, the data can be fed directly into the quantum circuit model in this approach and hence problems associated with data input and output prevalent in many of the quantum machine learning algorithms does not impact this implementation [29]. The developed algorithm is applied to the layered $\text{Li}_x\text{Co}_{2-x}\text{O}_2$ (LCO) system, used in Li-ion batteries, as a proof of concept demonstration. Computational advantages of this algorithm are explored and explained with an emphasis on two aspects: (i) reduction of the number of parameters and (ii) data anomaly detection. The significance of anomaly detection, especially for understanding of the magnetic interactions in the LCO system, is discussed.

* eunseok.lee@daimler.com

II. BACKGROUND

The energy of single-crystal materials can be expressed as a function of occupation variables σ_j , which indicate an atomic species on lattice site j . The total number of distinct configurations $\sigma = \sigma_1\sigma_2\cdots\sigma_N$ on N lattice sites will be m^N , where m is the number of different atomic species constituting the material, and thus m^N parameters will be required to build a complete model of energy as a function of σ , $E(\sigma)$, for all configurations $\{\sigma\}$. For example, a binary crystalline material with its atoms dispersed on N lattice sites will have 2^N distinct σ configurations that can be distinguished by 2^N parameters. If the force-field of the system is known to have an explicit formula as a function of continuous variables, e.g. pairwise potential as a function of interatomic distance, fewer number of parameters may be sufficient for modeling the energy. However, without such foreknowledge, in principle, m^N parameters are needed. In practice, the number of the required parameters are reduced by using intrinsic material properties and data-science techniques. One such technique is the cluster expansion method [30–34] where the energy is expanded in terms of atomic clusters and the corresponding expansion coefficients are used as the parameters to model the energy. Then, the parameters are truncated by considering rotational and translational symmetries of atomic clusters, assuming a cutoff distance for effective interactions between atoms, and iteratively searching for the most representative atomic clusters while leaving out the others (compromising the accuracy). Although these techniques have been demonstrated successfully in certain areas of materials research, in particular the area of battery materials [32, 34–36], there are still fundamental limits in increasing computational efficiency, due to the time-consuming process of sorting out the most representative parameters as well as the risk of deteriorated anomaly detection caused by incorrectly truncated parameters [37, 38].

III. APPROACH

We develop a hybrid quantum-classical algorithm to efficiently model the energy of a binary crystalline material as a function of σ ($\sigma_j = \pm 1$). A quantum circuit model can model complicated correlations in a data-set generated using quantum mechanical techniques. In our algorithm, a parameterized quantum circuit is trained by minimizing a cost function that measures the difference between the energies predicted from the quantum circuit and those computed via classical techniques. Once converged, the trained model will be capable of predicting the energy of arbitrary σ without performing classical energy calculations. Workflow of the proposed algorithm is as illustrated in FIG. 1.

Our design principle for quantum circuit assigns one qubit to each occupation variable and entangle every pair of the nearest neighbor qubits. While there can be several variants in arranging the entangling operators on a circuit, we adopted one with the circuit depth increasing linearly in the number of qubits for simplicity. The designed quantum circuit model consists of two consecutive layers of parameterized single and two qubit operations acting on N qubits where each layer is given by the following unitary transformation:

$$U(\{\vec{\Theta}\}, \sigma) = \exp\left(i \sum_{j=0}^{N-1} \phi_j \hat{X}_j\right) \exp\left(i \sum_{j=0}^{N-1} \theta_j \sigma_j \hat{Z}_j + i \sum_{j=0}^{N-2} \theta_{j,j+1} \sigma_j \sigma_{j+1} \hat{Z}_j \hat{Z}_{j+1}\right) \quad (1)$$

In Eq. (1), σ_j denotes the occupation variable on lattice site j , and \hat{X}_j and \hat{Z}_j denote the Pauli operators at the lattice site j . $\{\vec{\Theta}\} = \{\phi_j, \theta_j, \theta_{j,j+1}\}$ indicate the free parameters in the circuit to be learned. We use two consecutive layers of the unitary circuit presented in Eq. (1) to represent quantum chemical interactions in the lattice system. There are overall $6N - 2$ free parameters in this circuit for a lattice system with N lattice sites. Based on the results in [22, 39, 40], we believe that this circuit model would be hard to simulate classically. Refer to Appendix C for more discussion on the properties of the quantum circuit used. The overall structure of the designed quantum circuit is as illustrated in FIG. 2 and detailed circuit for a 4 lattice site system is provided in Appendix D. The energy of the lattice system for a given configuration σ is evaluated as the expectation value of the state $|\psi(\sigma)\rangle$ given in Eq. (2)

$$|\psi(\sigma, \{\vec{\Theta}^{n=1,2}\})\rangle = U(\{\vec{\Theta}^2\}, \sigma) H^{\otimes N} U(\{\vec{\Theta}^1\}, \sigma) H^{\otimes N} |0\rangle^{\otimes N} \quad (2)$$

with respect to the $\hat{X}_1 \hat{Y}_2 \cdots \hat{X}_{N-1} \hat{Y}_N$ operator using a quantum processing unit. Note that the $\hat{X}_1 \hat{Y}_2 \cdots \hat{X}_{N-1} \hat{Y}_N$ operator was chosen to reduce the effects from the unintentional parity-symmetries of occupation variables and hence to distinguish σ effectively (see Appendix C). Thus, the energy predicted by this model, E^{QC} , is:

$$E^{QC}(\sigma, \{\vec{\Theta}^{n=1,2}\}, s) = s \langle \psi(\sigma, \{\vec{\Theta}^{n=1,2}\}) | \hat{X}_1 \hat{Y}_2 \cdots \hat{X}_{N-1} \hat{Y}_N | \psi(\sigma, \{\vec{\Theta}^{n=1,2}\}) \rangle \quad (3)$$

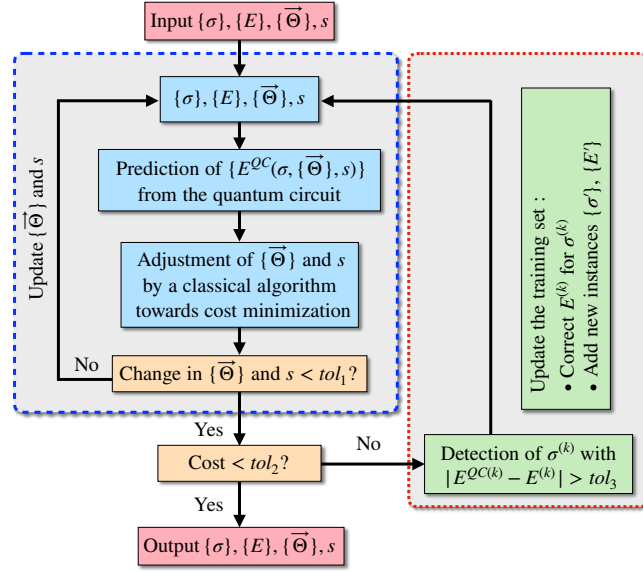


FIG. 1. Workflow of the proposed algorithm - σ and E are the configuration of occupation variables and the energy from classically-computed quantum chemical simulation (density functional theory calculation in this study), respectively, per each data instance. The parameters $\{\tilde{\Theta}\}$ and s , which are the coefficients of the quantum circuit and a scaling factor, respectively, are used to predict the energy E^{QC} for a given σ and optimized classically through minimization of a cost function. tol_1 and tol_2 are the thresholds to determine if the parameters were converged and the cost reached the minimum, respectively, while tol_3 is used to identify data instances with anomaly. $E^{QC(k)}$ and $E^{(k)}$ are the energies for the k -th configuration $\sigma^{(k)}$ in the training set. The training set is updated by correcting the anomalous data instances and adding new data instances. Variational quantum-classical optimization process and data anomaly detection process are denoted by blue-dashed and red-dotted regions, respectively.

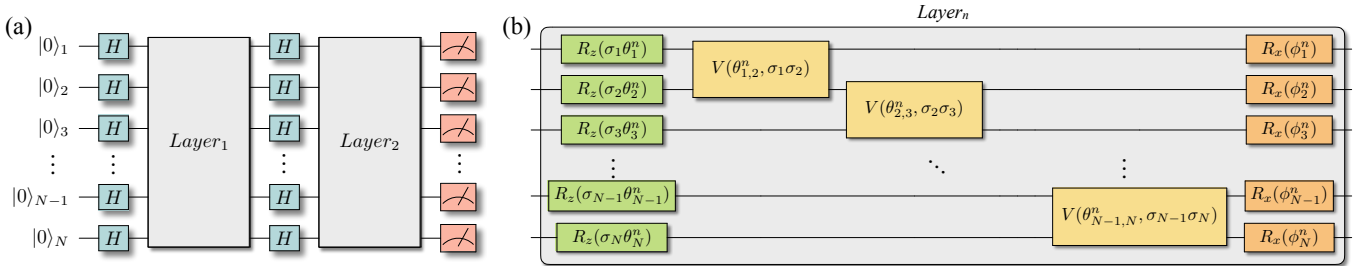


FIG. 2. Illustration of the proposed quantum circuit - (a) the entire circuit and (b) one layer. The circuit consists of a set of free parameters $\{\tilde{\Theta}^n\} = \{\theta_j^n, \theta_{j,j+1}^n, \phi_j^n\}$ where the subscript denotes the lattice site(s) and the superscript specifies the layer number. The two-qubit operator $V(\theta_{j,j+1}^n, \sigma_j \sigma_{j+1})$ denotes $e^{i\theta_{j,j+1}^n \sigma_j \sigma_{j+1} \hat{Z}_j \hat{Z}_{j+1}}$ and represents the entangling operator between qubits j and $j+1$ on the layer n .

In Eq. (3), we introduce a scaling factor, s , which is also an optimization parameter, to account for the overall scale of the predicted energies. With the inclusion of the scaling factor, the total number of parameters to be optimized is $6N - 1$. E^{QC} , as a function of σ , is then compared with the energy, obtained from classically-computed quantum chemical simulation. This algorithm was implemented using IBM's open source Qiskit Aqua software and the results were simulated using the statevector-simulator provided within Qiskit [41]. In this study, density functional theory (DFT) was used to calculate the energy classically, E^{DFT} . To help with the optimization procedure, the classical DFT energy data was pre-processed. Details of this procedure are outlined in Appendix A.

Data instances from the DFT calculations are divided into two sets, training set and test set. Both E^{QC} and E^{DFT} are obtained for all configurations in the training set. The coefficients ($\{\tilde{\Theta}^1\}, \{\tilde{\Theta}^2\}$) and the scaling parameter s are then optimized to minimize the cost, defined as the Root-Mean-Square-Error (RMSE) of the $E^{QC}(\sigma)$ compared with

the $E^{DFT}(\sigma)$ for each configuration σ in the training set, as follows.

$$cost = \sqrt{\sum_{i=1}^{N_{data}} \frac{(E^{QC(i)} - E^{DFT(i)})^2}{N_{data}}} \quad (4)$$

In Eq. (4), N_{data} is the number of data instances in the training set and i denotes the i^{th} data instance. This optimization process is carried out using a combination of Constrained Optimization BY Linear Approximation (COBYLA) [42] and Adaptive Moment Estimation (Adam) [43]. The COBYLA optimization algorithm is applied until the number of iterations for parameter optimization reach the preset maximum of 10,000, or the a preset error tolerance, tol_1 of less than 10^{-4} . In the former case, the optimization parameters are then refined further using Adam algorithm until the tolerance reaches tol_1 . After the completion of the optimization run (refer to FIG. 1), if the evaluated cost is found to be higher than a fixed value, tol_2 , all data instances used for training which show a discrepancy of greater than tol_3 between E^{QC} and E^{DFT} are examined by performing DFT calculations for the same σ but with updated DFT parameters, the initial values of magnetic moments in this study. If the E^{DFT} from the re-run DFT calculation is lower than the current value, the data point is replaced with new value in the training set. Otherwise, a new data instance is created by performing a DFT calculation for a similar σ and added to the training set. We refer to this process as anomaly detection and treatment (see Appendix B for more detail). The sequence of parameter optimization, anomaly detection and treatment (referred to as a round) is repeated until the obtained cost is less than a preset value $tol_2 = 0.03$ eV per cation (or 0.015 eV per atom). This value for tol_2 was adopted considering its ratio the variation of E^{DFT} in the training set to ensure the circuit can effectively distinguish the energies of distinct σ . tol_3 was set to be flexible during rounds; 0.1 eV per cation was used in initial rounds and then 0.06 eV per cation was used later.

The algorithm and quantum circuit are applied to the LCO system, a core component in one of widely used Li-ion battery cathodes, lithium Nickel-Manganese-Cobalt oxides, abbreviated as NMC. While the LCO system have been modeled in many previous computational research studies, its magnetic properties have been rarely studied due to difficulties in calculating magnetic moments precisely (refer to Appendix A). Anomaly detection and treatment process in our algorithm is expected to mediate these difficulties. Ideally, the layered LiCoO_2 (LCO at $x = 1$) consists of alternating cation (Li or Co) layers with one anion (O) layer between each cation layer. However, in our model cationic lattice sites are assumed to be occupied by either Li or Co, considering cations-intermixing, in particular, when the chemical composition of LCO deviates from $x = 1$. Oxygen atoms are assumed to reside in anion layers and, thus, only cationic lattice sites are assigned σ_j . While σ_j can have any value unless it nullifies the associated coefficients, we adopted +1 for Co and -1 for Li in this study, for convenience.

IV. RESULTS AND DISCUSSION

At first, the algorithm was applied to a 4 cationic lattice site LCO system. In the 4 lattice site system, the total number of possible configurations, $\{\sigma\}$, is 16. Therefore, in principle, 16 parameters should be sufficient to model the energy of the system. However, the spin-polarized DFT calculations (used in this study) often fail to converge to the ground state, especially for transition-metal oxides, and predict a number of different thermodynamically-meta-stable states for identical σ due to the slow convergence of magnetic moment (see Refs [36, 44–46]), producing many more than 2^N data instances for N lattice site system, including anomalous data instances due to unconverged magnetic moments. Thus, the anomaly detection and treatment process is essential for reliable modeling. In a parallel effort, we also modeled this 4 lattice site system classically (16 parameters was small enough for classical approaches) to provide a benchmark result for our algorithm. The parameters and expansion basis were formulated using the cluster expansion method without any truncation, and the same process as the anomaly detection and treatment in our algorithm was applied.

The training set used consisted of 30 data instances. Note that a few instances of the training set had identical σ but different energies due to distinct magnetic moments of ions, rendering the training on such an inconsistent data set inefficient. After the parameter optimization in the 1st round, the value of the cost function reduced to 0.10 eV/cation from the initial value of 0.38 eV/cation. We also observed that data instances that displayed a large discrepancy between E^{DFT} and E^{QC} were often not fully-converged for their magnetic moments. For example, a large $|E^{QC} - E^{DFT}|$ was observed for LiCoO_2 (LCO at $x = 1$) data instances with magnetic Co ions, while the oxidation state of Co ions at $x = 1$ is known to be Co^{3+} which is nonmagnetic. Those data instances with large $|E^{QC} - E^{DFT}|$ were updated by the procedure for anomaly detection and treatment (see Methods). This process was repeated to the fourth round and the resultant cost reduced to 0.018 eV/cation (or 0.009 eV/atom), corresponding to 1.55% of the variation of E^{DFT} in the training set, which ranged from -11.596 to -10.431 eV per cation. The corresponding mean

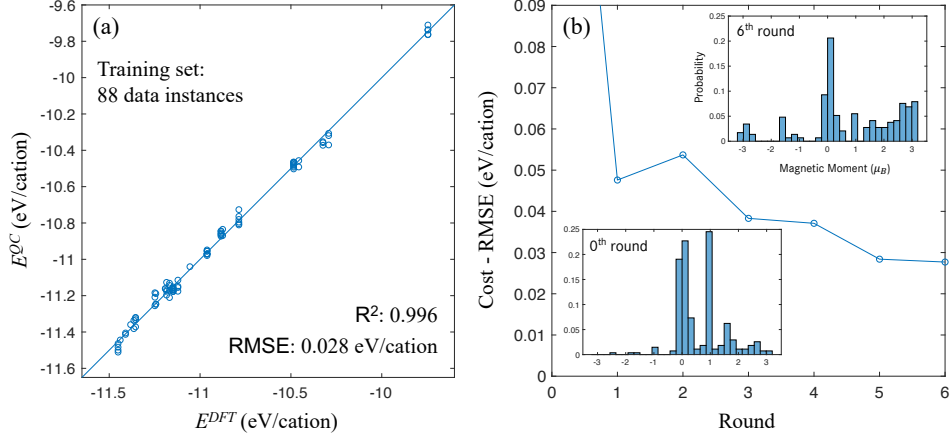


FIG. 3. (a) Comparison between E_i^{DFT} and E_i^{QC} for data instances in the training set for 8 cationic lattice site LCO system. RMSE and R^2 denote the resultant cost and the coefficient of determination, respectively. (b) The resultant cost after each round. The value at 0th round was adopted from the cost at the 1st step of the optimization of the parameters which started from random values. Two inset figures show the probability histogram of the magnetic moments of Co ions in the training set, obtained from DFT calculations using GGA+U scheme, at the 0th and the 6th rounds.

absolute percentage error (MAPE) was 0.096%. As stated earlier, we also modeled $E(\sigma)$ classically. The resultant cost was 0.12 eV/cation after the first round and then reduced to 0.018 eV/cation after the fourth round, which are almost the same as the result from our algorithm.

The algorithm was then applied to a 8 cationic lattice site LCO systems. As stated earlier, many more than 2^8 data instances can be produced from DFT calculations due to the slow convergence of magnetic moment. The initial training set had 72 data instances of randomly chosen and distinct σ . The anomaly detection and treatment process was then applied. After 6 rounds tolerance criterion for the cost function was met. The final size of the training set increased to 88 data instances and the resultant cost was 0.028 eV/cation. The performance of this training result can be assessed by comparing $E^{DFT(i)}$ and $E^{QC(i)}$, which is shown in FIG. 3(a). The cost 0.028 eV per cation corresponds to 1.58% of the variation in E^{DFT} values of the training set that ranged from -11.451 eV to -9.746 eV per cation. The corresponding MAPE was 0.20%. We remark that in our algorithm the energy of the system is not decomposed into the parameters of interatomic interaction energies which is typically required by classical approaches; where they are pre-truncated before fitting or selected via an iterative search process. Instead, our algorithm represents the energy of material system by a parameterized quantum circuit as a whole, avoiding the risk of severe pre-truncation of parameters and time-consuming iterative selection process. Modeling a system as a whole also brings computational efficiency in anomaly detection and treatment by reducing the risk of over-fitting to a specific set of (selected) parameters.

At the end of each round, we investigated if there was a relationship between the anomalous data and the chemical composition of materials. In general, $|E^{QC} - E^{DFT}|$ tended to be larger in the Co-rich region ($2 - x \geq 1.5$). This tendency is compatible with the fact that CoO, which is the LCO system with the highest Co content, has a cubic structure, clearly different from the hexagonal plane structure of the host LCO system. On the other hand, Li_2O_2 , the LCO system with the highest Li content, also has a different crystal structure from the LCO but still contains partial geometric similarities to the host LCO system, such as hexagonal planar structure and octahedral cationic sites in every other cation layers. Thus the geometric compatibility with the host LCO system may be less significant in the Li-rich region. See Appendix E for the illustration of their geometric structures. As explained in Methods, in the training, the energies of geometrically optimized structures are used. Thus, as the rounds proceed, the coefficients are trained to represent the energies of the structures which are more geometrically-compatible with the host LCO system. The result also infers that data instances can be grouped into roughly two regions, the Co-rich region and the other region, based on the geometric compatibility with host LCO system. Note that this grouping of data instances was learned through the rounds and not by a presumption on the geometric structure. This result can be considered as another evidence for the feasibility of the developed algorithm.

We also investigated how the magnetic moments changed with each round. The GGA+U scheme, which was employed in this study for DFT calculations, adds artificial Coulomb interaction of localized electrons manually and often fails to predict accurate magnetic moments, especially for transition-metal oxides [36, 47, 48]. Hence, the magnetic moments obtained in this study will be used only to estimate a general tendency, not exact magnetic interactions

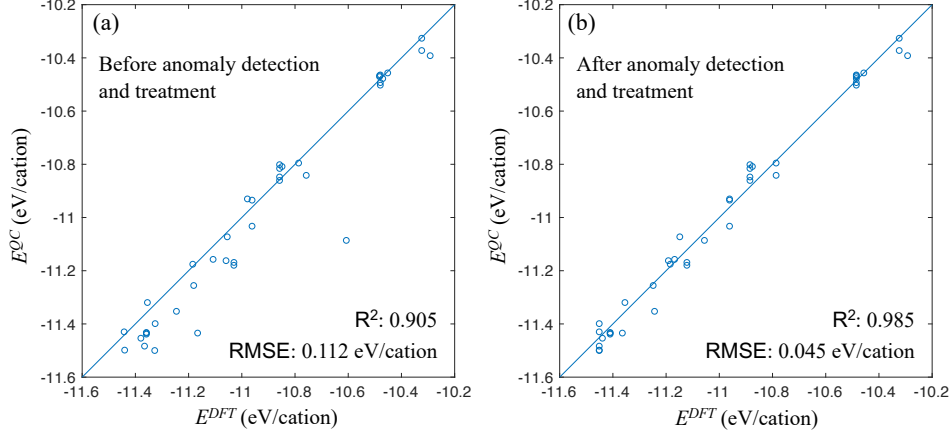


FIG. 4. Comparison between E_i^{DFT} and E_i^{QC} for data instances in the test set of the 8 cationic lattice site LCO system – (a) before and (b) after the anomaly detection and treatment were applied. RMSE and R^2 denote the resultant cost and the coefficient of determination, respectively.

between ions. Two inset figures in FIG. 3(b) show how magnetic moments of Co ions evolve as the rounds proceed. It is shown that the magnetic moment has values localized mostly around 0 or 1 at the 1st round while it is more dispersed after the 6th round. In particular, the population of $3\mu_B$ bin grows significantly. According to the one-to-one comparison of magnetic moment between GGA+U and hybrid-DFT calculations (using the HeydScuseriaErnzerhof (HSE) functional [49]), which provides more reliable value of magnetic moment, $3\mu_B$ from GGA+U corresponds to $0.11\mu_B$ from HSE while the ones less than $3\mu_B$ corresponds to zero [36]. The population of the data instances which have Co ions with greater than $3\mu_B$ magnetic moment was 2.7% and 18% of the training set at the 1st and the 6th round, respectively. This result implies that the magnetic moments of Co ions were predicted to be zero in most data instances in initial rounds but were corrected in later rounds by the anomaly detection and treatment process. It also suggests to consider magnetic interactions between Co ions to better understand the thermodynamic behaviors of the LCO system.

The optimized coefficients were then used to predict the energy for the test set (data instances that were not included to the training set), to investigate whether the optimization was over-fitted to the training set. As the incompatibility between the Co-rich region and the other regions was already indicated, all the data instances in the test set were for the ones with $2 - x < 1.5$. 40 data instances were prepared considering a typical ratio of the test set to the training set. The results are shown in FIG. 4. Although the cost was as high as 0.112 eV per cation without anomaly detection and treatment, it reduced to 0.045 eV per cation after the anomaly detection and treatment were applied. R^2 also increased from 0.905 to 0.985. The corresponding MAPE was 0.34%.

V. CONCLUSION AND OUTLOOK

In summary, we developed a heuristic quantum-classical algorithm to model the energy of substitutionally disordered binary crystalline materials as a function of atomic species on lattice sites via iterative learning based on the data of classically-computed quantum chemical simulation results but in quantum-enhanced feature space. We expect a quantum circuit model to be particularly suitable for representing data generated from a quantum mechanical system. The developed algorithm is expected to bring two computational advantages – the number of parameters increases linearly with the number of lattice sites and anomalous data can be detected and treated efficiently, as demonstrated on the LCO system. We remark that these advantages were possible because the energy of material systems is governed by only a few representative parameters while it is still computationally expensive to identify such parameters classically. Although it was demonstrated on relatively small size systems, the developed algorithm should be applicable to larger systems. We recognize that heuristic variational quantum-classical algorithms can face issues like barren plateaus [50] during the optimization process, these issues can however be addressed by using clever techniques of leveraging parameter values optimized for smaller systems when studying a larger system along with global optimizers. While in this study the anomaly of data was assessed using the magnetic moments of ions, other types of material properties, such as geometric distortion can be used as well. We believe this study encourages follow-up experimental study, running the algorithm on quantum computing hardware. In this case, the entangling

operators in the circuit are suggested to be rearranged (but within the same block of entangling operators) to satisfy conditions required for hardware experiments.

VI. ACKNOWLEDGMENTS

The authors thank Julia Rice (IBM) and Mario Motta (IBM) for useful discussions, suggestions and help with figures. A part of this research used resources of the National Energy Research Scientific Computing Center (NERSC), a U.S. Department of Energy Office of Science User Facility operated under Contract No. DE-AC02-05CH11231.

Appendix A: DFT Calculations of the LCO System

The layered Li-cobaltate system has $R\bar{3}m$ space group with alternating layers of Li and Co ions, as illustrated in FIG. 5. In this study, the same layered structure is adopted as the host structure of the LCO system but each lattice site is assumed to be occupied by either Li or Co ion without hard-separating Li and Co layers, considering the occurrence of cation-mixing. The supercell of the 4 cationic lattice site system was defined by taking the region illustrated in FIG. 5(a).

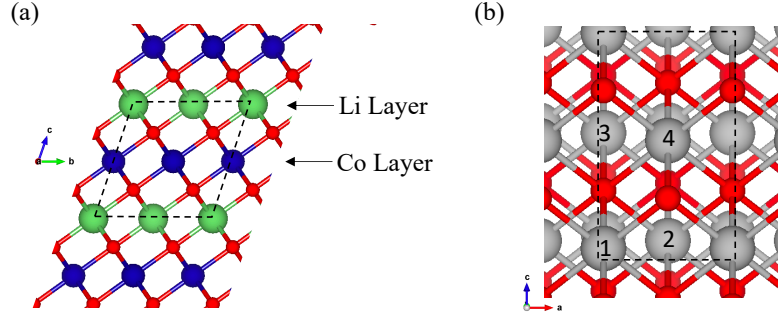


FIG. 5. Illustration of (a) the ideal structure of layered Li-cobaltate and (b) 4 cationic lattice sites used to define the supercell of the 4 cationic lattice site system. The supercell is also indicated by the regions enclosed by dashed lines. In (b), the cationic sites are colored gray because they are assumed to be occupied by either Li or Co.

The energies of the LCO system, E^{DFT} , were obtained classically with DFT using the generalized gradient approximation (GGA) with the Perdew-Burke-Ernzerhof parametrization [51], as implemented in Vienna Ab-initio Software Package (VASP) [52–55]. The +U scheme is employed to account for the effect from electron localization [56, 57], which is typical in transition metal oxides. U value of 3.4 is chosen for Co ions. A cutoff energy of 520 eV is used and the k-point mesh is adjusted to ensure convergence of 1 meV per atom. The volume and shape of the supercell are allowed to change during the relaxation. While Co ions in LiCoO_2 (the LCO at $x=1$) are in general known to be Co^{3+} and nonmagnetic, they may have different oxidation state and magnetic states at other compositions. Hence, the spin-polarized DFT calculations are performed in this study. The initial value of magnetic moment is given to each ion and allowed to change during the relaxation. In principle, the magnetic moments are supposed to be relaxed to the ones of the ground state regardless of the initial values. However, in practice, the relaxation of magnetic moments is very slow and several meta-stable states can be predicted for one identical σ [36, 44–46], creating anomalous data. In this study, we assigned 0.05 for the initial values of magnetic moment. After the calculation is finished, the value of σ_j is determined by the species of the atom located within a certain distance from the lattice site j . We used 0.35 Å for that distance in this study; the distance between the nearest neighbor cations is around 2.85 Å in the LCO system. Although E^{DFT} can be used directly in the optimization, in general the optimization becomes more efficient when the scale of variation in training values is smaller. For this purpose, $xE_{Li}^0 + (1-x)E_{Co}^0$ is subtracted from E^{DFT} (eV per cation) and then used during the optimization of the circuit parameters. Note that E_{Li}^0 and E_{Co}^0 are not reference energies but artificially-designed factors to disperse the converted E^{DFT} evenly in $[-,+]$ range. In this study, E_{Li}^0 and E_{Co}^0 are set to -10.39 eV and -11.65 eV, respectively. Once the parameters are optimized, $xE_{Li}^0 + (1-x)E_{Co}^0$ are added back to the values evaluated from the circuit to convert to E^{QC} (eV per cation).

Appendix B: Anomaly Treatment

Each data instance with large $|E^{QC} - E^{DFT}|$ is addressed by performing additional DFT calculations and treated according to the following procedure.

1. One DFT calculation is performed continuing from the previous DFT calculation results, the geometry of the supercell, the atoms' position, and the magnetic moments, to confirm that there were no numerical artifacts in the previous DFT calculation.
2. DFT calculations are performed again with the magnetic moments initialized to values from the ones in previous DFT calculation. If the energy returned is lower, the data point is updated in the training set, i.e. the old energy is replaced with the new energy.
3. If lower energy is not predicted from the second step, DFT calculation is performed for a new σ with a single lattice site, σ_j , altered. The altered lattice site is selected randomly. This new data instance is then added to the training set.

The second step was essential for this study, because the LCO system contains transition-metal ions which we believe are affected significantly by magnetic interactions if magnetized. During the initial rounds, we considered the surrounding Li ions on the same layer to select the best candidates for initial magnetic moment of Co ions. For example, if Co ions fully occupy one layer, those Co ions will be likely to have Co^{3+} oxidation state, which is non-magnetic. In this case, 0.05 initial magnetic moment was assigned to Co ions which were predicted to have non-zero magnetic moment from previous DFT calculation. On the other hand, if Co ions share the layer with Li ions, the oxidation state of those Co ions may be different from 3+. In this case, the Co ions were assigned 1.05 and 3.05 if they were predicted to be 0.05 from previous DFT calculation. In the later rounds, the correlation between the distribution of Co ions and their magnetic moments tended to be manifest and thus we adopted those values. The second step may be less significant in the modeling of nonmagnetic materials.

Appendix C: Properties of the Quantum Circuit

One-qubit and two-qubit operators in the proposed circuit are used to represent the interactions from atomic clusters. For example, the interaction energy of pair cluster $\sigma_1\sigma_2$ can be explained directly by $\text{ENT}(q_1, q_2)$, which indicates the entanglement between qubit 1 and qubit 2, while the interaction energy of $\sigma_1\sigma_3$ cluster can be explained indirectly by a combination of entanglements $\text{ENT}(q_3, \text{ENT}(q_1, q_2))$ and $\text{ENT}(q_2, q_3)$.

As the occupation variables are encoded in Z -axis only, rotations along the X -axis, R_X operators, are also added to provide more degrees of freedom. The inclusion of an additional layer of the single and two qubit operators will provide more degrees of freedom and entanglement to generate a richer feature space for describing the energy of the system. The quantum circuit ansatz used is also chosen to be hardware efficient for a system made of superconducting qubits with predominantly linear connectivity.

The choice of the operator $X_1Y_2X_3 \cdots X_{N-1}Y_N$ for estimating the energy of the system was made to overcome the inherent parity symmetries in different configurations since σ_i takes values of ± 1 only. For example, operator with tensor product of all Z operators for N qubits would not be able to distinguish between configurations having equal number of $+1$ s. Another suitable choice for the measurement operators would be to randomly pick one of the three Pauli operators for each lattice site and keep it fixed throughout the implementation. Note that, here we have chosen a single operator to estimate the energy, a linear combination of multiple N qubit operators can also be used but may require additional optimization parameters.

The coefficients in the proposed circuit should be able to distinguish the different set of occupation variables effectively. This test is conducted by calculating $E^{QC}(\sigma)$ while varying σ and the value of one coefficient in the range of $[0, 2\pi]$ (other coefficients are fixed to 1.0). If a coefficient produces a same constant outcome for all the σ 's, it will fail to distinguish between different σ . Note that the existence of a constant coefficient is acceptable because it can be used to account for the reference energy, linear terms, and background errors. We examined 9 different σ 's: $\bar{1}\bar{1}\bar{1}\bar{1}\bar{1}\bar{1}\bar{1}\bar{1}$, $1\bar{1}\bar{1}\bar{1}\bar{1}\bar{1}\bar{1}\bar{1}$, $\bar{1}\bar{1}\bar{1}\bar{1}\bar{1}\bar{1}1$, $\bar{1}\bar{1}\bar{1}\bar{1}1\bar{1}\bar{1}$, $\bar{1}\bar{1}\bar{1}1\bar{1}\bar{1}\bar{1}$, $\bar{1}\bar{1}1\bar{1}\bar{1}\bar{1}\bar{1}$, $\bar{1}1\bar{1}\bar{1}\bar{1}\bar{1}\bar{1}$, $1\bar{1}\bar{1}\bar{1}\bar{1}\bar{1}\bar{1}$, $11\bar{1}\bar{1}\bar{1}\bar{1}\bar{1}\bar{1}$ where $\bar{1}$ represents -1. The results are illustrated in FIG. 6. It is shown that each parameter produces different values of E^{QC} for different value of occupation variables, which illustrates its capability to distinguish distinct σ effectively. There are four constant coefficients which produce a constant E^{QC} in the entire range $[0, 2\pi]$, however, we remark that those constants vary with σ 's.

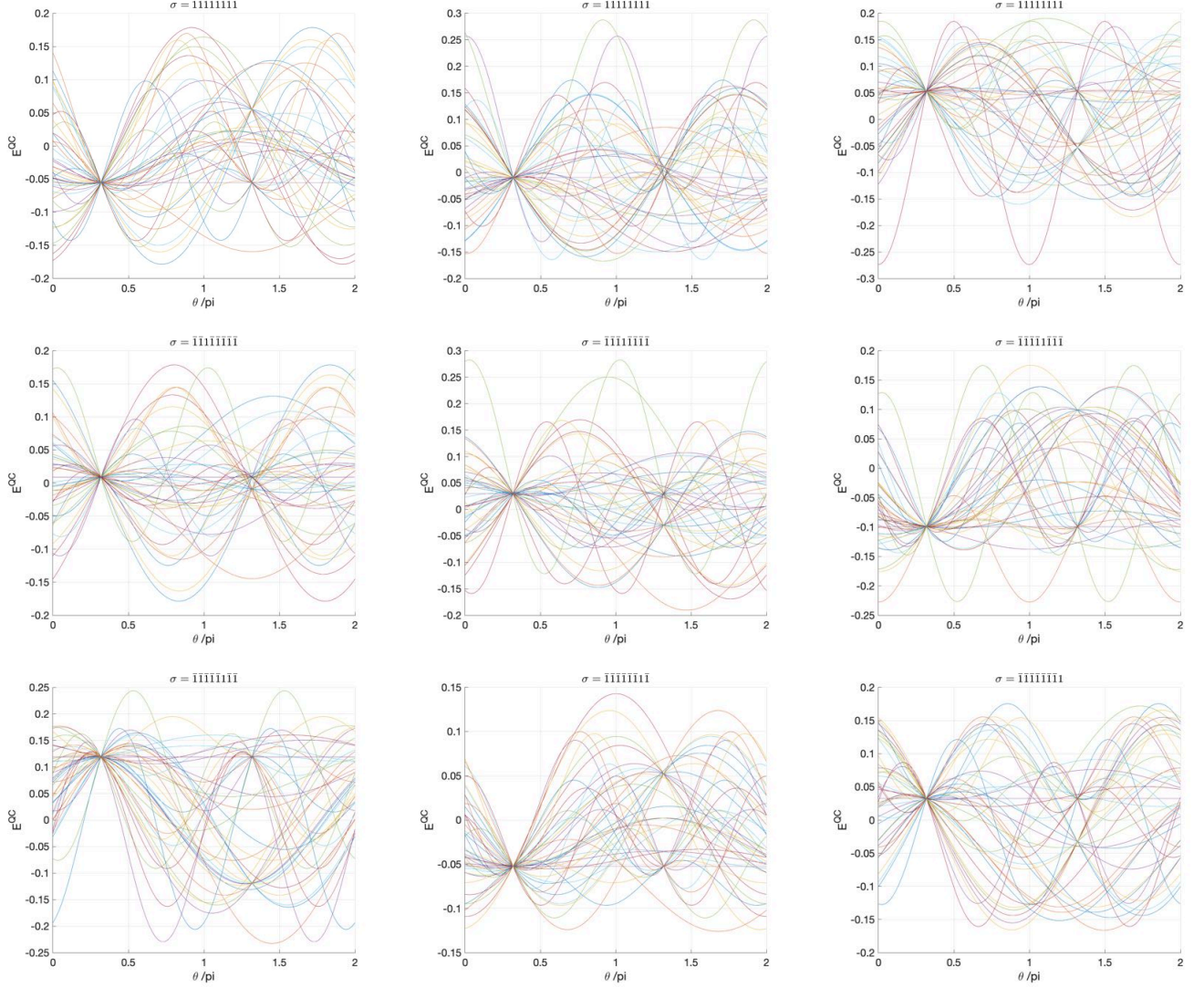


FIG. 6. Variation of the individual parameters of the circuit for a sample of different 8 lattice site configurations. The energy of the system is calculated by fixing every parameter except for one. This is implemented for every parameter. Different colors in the above plots correspond to the free parameters of the circuit.

Appendix D: Detailed representation of the quantum circuit

In FIG. 7, we provide, as an example, the representation of the circuit used for the 4 lattice site system. A similarly constructed 8 qubit circuit was used for the 8 lattice site system.

Appendix E: Crystal structures of the LCO system

The host LCO structure has a layered structure with alternating cation (Li or Co) layers with one anion (O) layer placed between each cation layer. Cations are located on octahedral sites and they are arranged forming a hexagonal plane. In the ideal LCO system at $x = 1$, Li and Co layers are clearly separated as illustrated in FIG. 8.

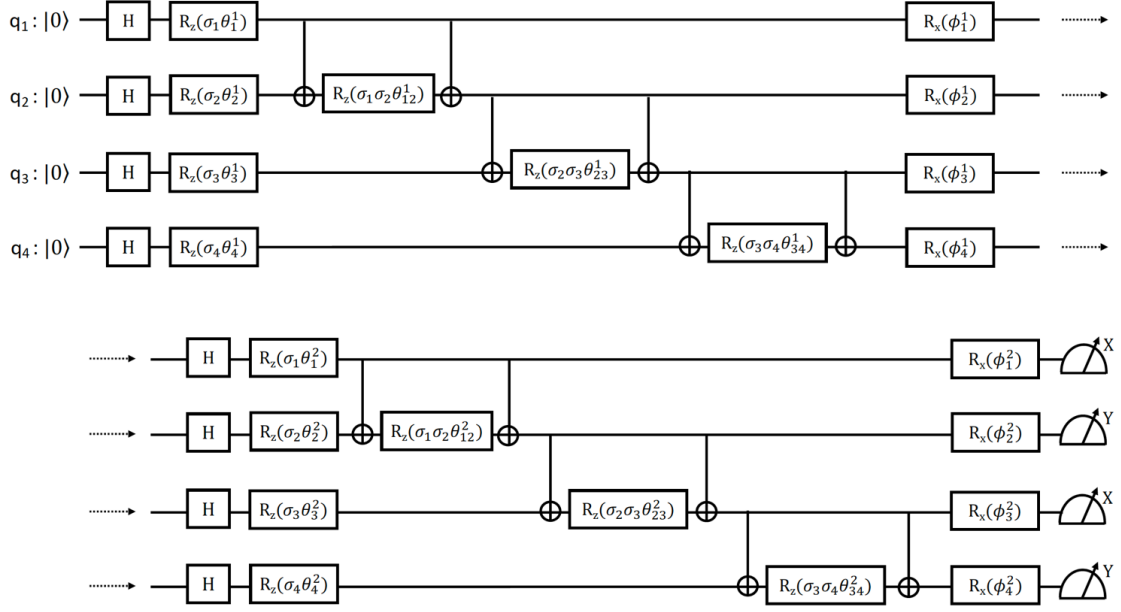


FIG. 7. Detailed illustration of the quantum circuit used for a 4 lattice site system. H represents Hadamard gates, R_x and R_z are rotations along the X and the Z axis respectively with the specified angles in brackets.

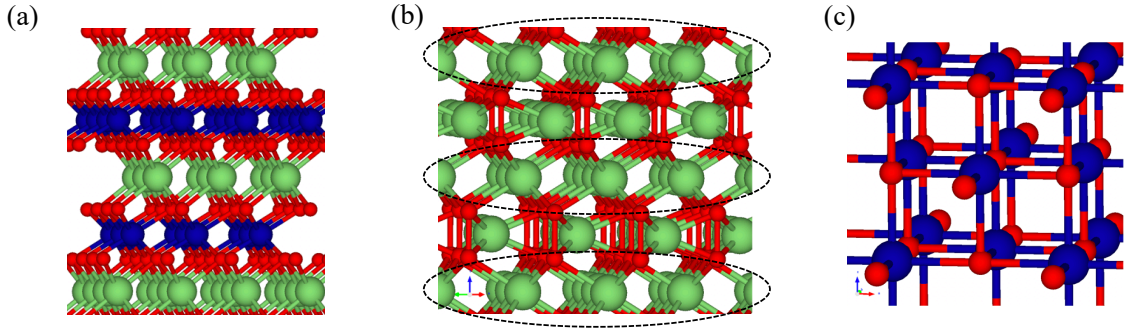


FIG. 8. Illustration of the crystal structures of the LCO systems used in the training - (a) the ideal LiCoO_2 , (b) Li_2O_2 , and (c) CoO . In (b), the dashed oval regions are to indicate LiO_6 or CoO_6 octahedra arranged toward a hexagonal cation distribution on the basal plane, a partial geometric-similarity between the LiCoO_2 and Li_2O_2 .

-
- [1] L. Ward and C. Wolverton, Current Opinion in Solid State and Materials Science **21**, 167 (2017).
 - [2] R. Gómez-Bombarelli, Chem **4**, 1189 (2018).
 - [3] G. Pilania, C. Wang, X. Jiang, S. Rajasekaran, and R. Ramprasad, Scientific reports **3**, 2810 (2013).
 - [4] A. Jain, S. P. Ong, G. Hautier, W. Chen, W. D. Richards, S. Dacek, S. Cholia, D. Gunter, D. Skinner, G. Ceder, and K. A. Persson, APL Materials **1**, 011002 (2013).
 - [5] S. Kirklin, J. E. Saal, B. Meredig, A. Thompson, J. W. Doak, M. Aykol, S. Rühl, and C. Wolverton, npj Computational Materials **1** (2015), 10.1038/npjcompumats.2015.10.
 - [6] R. Ramprasad, R. Batra, G. Pilania, A. Mannodi-Kanakkithodi, and C. Kim, npj Computational Materials **3** (2017), 10.1038/s41524-017-0056-5, arXiv:1707.07294.
 - [7] Y. Huang, J. Kang, W. A. Goddard, and L.-W. Wang, Phys. Rev. B **99**, 064103 (2019).
 - [8] K. T. Schütt, F. Arbabzadah, S. Chmiela, K. R. Müller, and A. Tkatchenko, Nature Communications **8**, 6 (2017), arXiv:1609.08259.
 - [9] H. Xu, Y. Yu, Z. Wang, and G. Shao, ENERGY & ENVIRONMENTAL MATERIALS **2**, 234 (2019), <https://onlinelibrary.wiley.com/doi/pdf/10.1002/eem2.12053>.

- [10] S. Kirklin, B. Meredig, and C. Wolverton, *Advanced Energy Materials* **3**, 252 (2013), <https://onlinelibrary.wiley.com/doi/pdf/10.1002/aenm.201200593>.
- [11] D. Xue, P. V. Balachandran, J. Hogden, J. Theiler, D. Xue, and T. Lookman, *Nature Communications* **7**, 1 (2016).
- [12] J. Hill, G. Mulholland, K. Persson, R. Seshadri, C. Wolverton, and B. Meredig, *MRS Bulletin* **41**, 399 (2016).
- [13] T. Lookman, P. V. Balachandran, D. Xue, J. Hogden, and J. Theiler, *Current Opinion in Solid State and Materials Science* **21**, 121 (2017).
- [14] K. Takahashi and Y. Tanaka, *Dalton Trans.* **45**, 10497 (2016).
- [15] K. Temme, S. Bravyi, and J. M. Gambetta, *Physical Review Letters* **119**, 1 (2017), arXiv:1612.02058.
- [16] J. I. Colless, V. V. Ramasesh, D. Dahlen, M. S. Blok, M. E. Kimchi-Schwartz, J. R. McClean, J. Carter, W. A. De Jong, and I. Siddiqi, *Physical Review X* **8**, 11021 (2018), arXiv:1707.06408.
- [17] Y. Li and S. C. Benjamin, *Physical Review X* **7**, 1 (2017), arXiv:1611.09301.
- [18] E. Farhi, J. Goldstone, and S. Gutmann, <https://arxiv.org/abs/1411.4028>, 1 (2014), arXiv:1411.4028.
- [19] J. R. McClean, J. Romero, R. Babbush, and A. Aspuru-Guzik, *New Journal of Physics* **18** (2016), 10.1088/1367-2630/18/2/023023, arXiv:1509.04279.
- [20] K. Mitarai, M. Negoro, M. Kitagawa, and K. Fujii, *Phys. Rev. A* **98**, 032309 (2018).
- [21] A. Kandala, A. Mezzacapo, K. Temme, M. Takita, M. Brink, J. M. Chow, and J. M. Gambetta, *Nature* **549**, 242 (2017), arXiv:1704.05018.
- [22] V. Havlíček, A. D. Córcoles, K. Temme, A. W. Harrow, A. Kandala, J. M. Chow, and J. M. Gambetta, *Nature* **567**, 209 (2019).
- [23] A. Peruzzo, J. McClean, P. Shadbolt, M. H. Yung, X. Q. Zhou, P. J. Love, A. Aspuru-Guzik, and J. L. O'Brien, *Nature Communications* **5** (2014), 10.1038/ncomms5213, arXiv:1304.3061.
- [24] A. Kandala, K. Temme, A. D. Córcoles, A. Mezzacapo, C. J. M., and J. M. Gambetta, *Nature*, 491 (2019).
- [25] Q. Gao, H. Nakamura, T. P. Gujarati, G. O. Jones, J. E. Rice, S. P. Wood, M. Pistoia, J. M. Garcia, and N. Yamamoto, (2018), arXiv:1906.10675.
- [26] J. Preskill, *Quantum* **2**, 79 (2018), arXiv:1801.00862.
- [27] F. Arute, K. Arya, R. Babbush, D. Bacon, J. C. Bardin, R. Barends, R. Biswas, S. Boixo, F. G. Brandao, D. A. Buell, B. Burkett, Y. Chen, Z. Chen, B. Chiaro, R. Collins, W. Courtney, A. Dunsworth, E. Farhi, B. Foxen, A. Fowler, C. Gidney, M. Giustina, R. Graff, K. Guerin, S. Habegger, M. P. Harrigan, M. J. Hartmann, A. Ho, M. Hoffmann, T. Huang, T. S. Humble, S. V. Isakov, E. Jeffrey, Z. Jiang, D. Kafri, K. Kechedzhi, J. Kelly, P. V. Klimov, S. Knysh, A. Korotkov, F. Kostitsa, D. Landhuis, M. Lindmark, E. Lucero, D. Lyakh, S. Mandrà, J. R. McClean, M. McEwen, A. Megrant, X. Mi, K. Michielsen, M. Mohseni, J. Mutus, O. Naaman, M. Neeley, C. Neill, M. Y. Niu, E. Ostby, A. Petukhov, J. C. Platt, C. Quintana, E. G. Rieffel, P. Roushan, N. C. Rubin, D. Sank, K. J. Satzinger, V. Smelyanskiy, K. J. Sung, M. D. Trevithick, A. Vainsencher, B. Villalonga, T. White, Z. J. Yao, P. Yeh, A. Zalcman, H. Neven, and J. M. Martinis, *Nature* **574**, 505 (2019), arXiv:1911.00577.
- [28] E. Pednault, J. A. Gunnels, G. Nannicini, L. Horesh, and R. Wisnieff, (2019), arXiv:1910.09534.
- [29] J. Biamonte, P. Wittek, N. Pancotti, P. Rebentrost, N. Wiebe, and S. Lloyd, *Nature* **549**, 195 (2017).
- [30] J. M. Sanchez and D. de Fontaine, in *AIP Conference Proceedings*, Vol. 53 (AIP, 1979) pp. 133–145.
- [31] C. Wolverton and D. de Fontaine, *Physical Review B* **49**, 8627 (1994).
- [32] M. Asta, V. Ozolins, and C. Woodward, *JOM* **53**, 16 (2001).
- [33] A. Van der Ven, H.-C. Yu, G. Ceder, and K. Thornton, *Progress in Materials Science* **55**, 61 (2010).
- [34] E. Lee and K. A. Persson, *Nano Letters* **12**, 4624 (2012).
- [35] K. Persson, V. a. Sethuraman, L. J. Hardwick, Y. Hinuma, Y. S. Meng, A. van der Ven, V. Srinivasan, R. Kostecki, and G. Ceder, *The Journal of Physical Chemistry Letters* **1**, 1176 (2010).
- [36] E. Lee, H. Iddir, and R. Benedek, *Physical Review B* **95**, 085134 (2017).
- [37] V. Chandola, A. Banerjee, and V. Kumar, *ACM Comput. Surv.* **41** (2009), 10.1145/1541880.1541882.
- [38] R. Chalapathy and S. Chawla, “Deep learning for anomaly detection: A survey,” (2019), arXiv:1901.03407 [cs.LG].
- [39] S. Bravyi, D. Gosset, and R. König, *Science* **362**, 308 (2018), <https://science.sciencemag.org/content/362/6412/308.full.pdf>.
- [40] S. Bravyi, D. Gosset, and R. Movassagh, Preprint at Arxiv, 1 (2019), arXiv:1909.11485.
- [41] H. Abraham, I. Y. Akhalwaya, G. Aleksandrowicz, T. Alexander, G. Alexandrowics, E. Arbel, A. Asfaw, C. Azaustre, AzizNgoueya, P. Barkoutsos, G. Barron, L. Bello, Y. Ben-Haim, D. Bevenius, L. S. Bishop, S. Bosch, S. Bravyi, D. Bucher, F. Cabrera, P. Calpin, L. Capelluto, J. Carballo, G. Carrascal, A. Chen, C.-F. Chen, R. Chen, J. M. Chow, C. Claus, C. Clauss, A. J. Cross, A. W. Cross, S. Cross, J. Cruz-Benito, C. Culver, A. D. Córcoles-Gonzales, S. Dague, T. E. Dandachi, M. Dartiaill, DavideFrr, A. R. Davila, D. Ding, J. Doi, E. Drechsler, Drew, E. Dumitrescu, K. Dumon, I. Duran, K. EL-Safty, E. Eastman, P. Eendebak, D. Egger, M. Everitt, P. M. Fernández, A. H. Ferrera, A. Frisch, A. Fuhrer, M. GEORGE, J. Gacon, Gadi, B. G. Gago, J. M. Gambetta, A. Gammanpila, L. Garcia, S. Garion, J. Gomez-Mosquera, S. de la Puente González, I. Gould, D. Greenberg, D. Grinko, W. Guan, J. A. Gunnels, I. Haide, I. Hamamura, V. Havlicek, J. Hellmers, L. Herok, S. Hillmich, H. Horii, C. Howington, S. Hu, W. Hu, H. Imai, T. Imamichi, K. Ishizaki, R. Iten, T. Itoko, A. Javadi-Abhari, Jessica, K. Johns, T. Kachmann, N. Kanazawa, Kang-Bae, A. Karazeev, P. Kassebaum, S. King, Knabberjoe, A. Kovyshin, V. Krishnan, K. Krsulich, G. Kus, R. LaRose, R. Lambert, J. Latone, S. Lawrence, D. Liu, P. Liu, Y. Maeng, A. Malyshev, J. Marecek, M. Marques, D. Mathews, A. Matsuo, D. T. McClure, C. McGarry, D. McKay, S. Meesala, M. Mevissen, A. Mezzacapo, R. Midha, Z. Minev, N. Moll, M. D. Mooring, R. Morales, N. Moran, P. Murali, J. Muggenburg, D. Nadlinger, G. Nannicini, P. Nation, Y. Naveh, P. Neuweiler, P. Niroula, H. Norlen, L. J. O’Riordan, O. Ogunbayo, P. Ollitrault, S. Oud, D. Padilha, H. Paik, S. Perriello, A. Phan, M. Pistoia, A. Pozas-iKerstjens, V. Prutyayov, D. Puzzuoli, J. Pérez, Quintiii, R. Raymond, R. M.-C. Redondo, M. Reuter, J. Rice, D. M. Rodríguez,

- M. Rossmannek, M. Ryu, T. SAPV, SamFerracin, M. Sandberg, N. Sathaye, B. Schmitt, C. Schnabel, Z. Schoenfeld, T. L. Scholten, E. Schoute, I. F. Sertage, K. Setia, N. Shammah, Y. Shi, A. Silva, A. Simonetto, N. Singstock, Y. Siraichi, I. Sitdikov, S. Sivarajah, M. B. Sletfjerdings, J. A. Smolin, M. Soeken, I. O. Sokolov, D. Steenken, M. Stypulkoski, H. Takahashi, I. Tavernelli, C. Taylor, P. Taylour, S. Thomas, M. Tillet, M. Tod, E. de la Torre, K. Trabing, M. Treinish, TrishaPe, W. Turner, Y. Vaknin, C. R. Valcarce, F. Varchon, A. C. Vazquez, D. Vogt-Lee, C. Vuillot, J. Weaver, R. Wiczorek, J. A. Wildstrom, R. Wille, E. Winston, J. J. Woehr, S. Woerner, R. Woo, C. J. Wood, R. Wood, S. Wood, J. Wootton, D. Yeralin, R. Young, J. Yu, C. Zachow, L. Zdanski, C. Zoufal, Zoufalc, azulehner, bcamorrison, brandhsn, chlorophyll zz, dime10, drholmie, elfrocampeador, faisaldebouni, fanizzamarco, gruu, kanejess, klinvill, kurarr, lerongil, ma5x, merav aharoni, ordmoj, sethmerkel, strickroman, sumitpuri, tigerjack, toural, vvilpas, willhbang, yang.luh, and yotamvakinibm, “Qiskit: An open-source framework for quantum computing,” (2019).
- [42] A. R. Conn, K. Scheinberg, and P. Toin, in *Approximation Theory and Optimization: Tributes to M.J.D. Powell*, edited by M. Buhmann and A. Iserles (Cambridge University Press, 1997) pp. 83–108.
- [43] D. P. Kingma and J. L. Ba, in *3rd International Conference on Learning Representations, ICLR 2015 - Conference Track Proceedings* (2015) pp. 1–15, arXiv:1412.6980.
- [44] R. Zeller, Computational nanoscience: do it yourself! **31**, 419 (2006).
- [45] J. M. Wills, M. Alouani, P. Andersson, A. Delin, O. Eriksson, and O. Grechnev, *Full-Potential Electronic Structure Method: Energy and Force Calculations with Density Functional and Dynamical Mean Field Theory* (Springer Science & Business Media, 2010) p. 133.
- [46] G. Bihlmayer, in *Handbook of Materials Modeling*, edited by W. Andreoni and S. Yip (Springer, Cham, 2018) pp. 1–23.
- [47] F. Zhou, T. Maxisch, and G. Ceder, Physical Review Letters **97**, 155704 (2006).
- [48] J. Ren and R. Zhang, Progress in Natural Science: Materials International **29**, 362 (2019), special Issue of Computational Materials.
- [49] J. Heyd, G. E. Scuseria, and M. Ernzerhof, The Journal of Chemical Physics **118**, 8207 (2003).
- [50] J. R. McClean, S. Boixo, V. N. Smelyanskiy, R. Babbush, and H. Neven, Nature Communications **9**, 1 (2018), arXiv:1803.11173.
- [51] J. P. Perdew, K. Burke, and M. Ernzerhof, Physical Review Letters **78**, 1396 (1997).
- [52] G. Kresse and J. Hafner, Physical Review B **49**, 14251 (1994).
- [53] G. Kresse and J. Hafner, Phys. Rev. B **47**, 558 (1993).
- [54] G. Kresse and J. Furthmüller, Physical Review B **54**, 11169 (1996).
- [55] G. Kresse and J. Furthmüller, Computational Materials Science **6**, 15 (1996), arXiv:0927-0256(96)00008 [10.1016].
- [56] S. L. Dudarev, G. A. Botton, S. Y. Savrasov, C. J. Humphreys, and A. P. Sutton, Phys. Rev. B **57**, 1505 (1998).
- [57] A. I. Liechtenstein, V. I. Anisimov, and J. Zaanen, Phys. Rev. B **52**, R5467 (1995).